spacings that match the observation of the smaller arcs. Conversely, we note that if the arcs' current mean motion did not differ from that of the CIR, that is, if there were no observed offset, the CER is still the only resonance that can both confine the arcs and explain the longer radial structures; the required mass for shifting the CER to the CIR location can be found in Fig. 2.

The ring mass we determined, $0.002m_G$ assuming $e_G = 10^{-6}$, corresponds to a parent 10-km-radius satellite with a density similar to Galatea's. We note that many of our results can be reproduced in the case of a massless arc system if a second satellite shares its orbit. A similar model was put forward shortly after the discovery of the ring arc system but prior to Voyager's more detailed observations[16]. A closer inspection of this two-satellite model however shows that the second satellite would produce a single continuous arc at each equilibrium point (L_4 or L_5), leaving the sequence of small arcs unexplained. A satellite co-orbital to the arcs of mass $0.002m_G$ would activate the CER, which in turn modifies the satellite's potential near L_4 and L_5 to allow a structure similar to the arcs. However, Voyager data exclude[9] undetected satellites of radius larger than 6 km implying that the mass required for the angular confinement of the arcs is not contained in a single body. Modelling the breakup of an arc parent satellite[10,11] should henceforth include the dynamical effects described in this paper in order to ascertain the angular distribution of mass and solve the problem of radial stability of the arcs. If the torques exerted by Galatea on the arcs work like those in Saturn's rings[12,13], the rate of radial migration of the arcs is $2.4 \, \text{km yr}^{-1}$, disrupting the arcs in less than a year. However, the satellite's torque is less likely to cause a significant drift in the arcs' radial position if the rings' mass is concentrated in a few clumps.

The value estimated here for Galatea's eccentricity, about 10^{-6}, is consistent with the requirement that the arcs have a small mass, regardless of the physical model responsible for their angular confinement. The fact that the current spread in semi-major axis of the arcs leads to such a small eccentricity is encouraging, because we expect that the decay timescale of Galatea's eccentricity due to the tides raised by Neptune[1] is of the order of 10^8 years, implying a rapid circularization of the orbit over the age of the Solar System. More precise measurements of Galatea's orbital elements, as well as models of the tidal evolution of the inner neptunian satellites together with the ring–Galatea interaction[13], are needed to fully validate the resonance model presented here and determine the origin of the small residual eccentricity in Galatea's orbit responsible for the arcs' confinement. □

1. Goldreich, P., Tremaine, S. & Borderies, N. Towards a theory for Neptune's arc rings. *Astron. J.* **92**, 490–494 (1986).
2. Porco, C. An explanation for Neptune's ring arcs. *Science* **400**, 995–1001 (1991).
3. Dumas, C. *et al.* Stability of Neptune's arcs in question. *Nature* **400**, 733–735 (1999).
4. Sicardy, B. *et al.* Images of Neptune's ring arcs obtained by a ground-based telescope. *Nature* **400**, 731–733 (1999).
5. Dumas, C. *et al.* Astrometry and near infra-red photometry of Neptune's inner satellites and ring arcs. *Astron. J.* (in the press).
6. Nicholson, P. D., Mosquiera, I. & Matthews, K. Stellar occultation observations of Neptune's rings: 1984–1988. *Icarus* **113**, 295–330 (1995).
7. Owen, W. M., Vaughan, R. M. & Synnott, S. P. Orbits of the six new satellites of Neptune. *Astron. J.* **101**, 1511–1515 (1991).
8. Porco, C. *et al.* in *Neptune and Triton* (ed. Cruikshank, D. P.) 703–804 (Univ. Arizona Press, Tucson, 1995).
9. Smith, B. A. *et al.* Voyager 2 and Neptune: Imaging science results. *Science* **246**, 1422–1449 (1989).
10. Colwell, J. E. & Esposito, L. W. A model for dust production for Neptune's ring system. *Geophys. Res. Lett.* **17**, 1741–1744 (1990).
11. Colwell, J. E. & Esposito, L. W. Origin of the rings of Neptune and Uranus: II Initial conditions and ring moon population. *J. Geophys. Res.* **98**, 7387–7401 (1993).
12. Goldreich, P. & Tremaine, S. The dynamics of planetary rings. *Annu. Rev. Astron. Astrophys.* **20**, 249–283 (1982).
13. Namouni, F. Ringlet-satellite interactions. *Mon. Not. R. Astron. Soc.* **300**, 915–930 (1998).
14. Horanyi, M. & Porco, C. Where exactly are the arcs of Neptune? *Icarus* **106**, 525–535 (1993).
15. Hänninen, J. & Porco, C. Collisional simulations of Neptune's ring arcs. *Icarus* **126**, 1–27 (1997).
16. Lissauer, J. J. Shepherding model for Neptune's arc ring. *Nature* **318**, 544–545 (1985).

....

Towards Bose–Einstein condensation of excitons in potential traps

L. V. Butov*, C. W. Lai*, A. L. Ivanov†, A. C. Gossard‡ & D. S. Chemla*§

* *Materials Sciences Division, E. O. Lawrence Berkeley National Laboratory;*
§ *Department of Physics, University of California at Berkeley, Berkeley, California 94720, USA*
† *Department of Physics and Astronomy, Cardiff University, Cardiff CF24 3YB, UK*
‡ *Department of Electrical and Computer Engineering, University of California, Santa Barbara, California 93106, USA*

An exciton is an electron–hole bound pair in a semiconductor. In the low-density limit, it is a composite Bose quasi-particle, akin to the hydrogen atom[1]. Just as in dilute atomic gases[2,3], reducing the temperature or increasing the exciton density increases the occupation numbers of the low-energy states leading to quantum degeneracy and eventually to Bose–Einstein condensation (BEC)[1]. Because the exciton mass is small—even smaller than the free electron mass—exciton BEC should occur at temperatures of about 1 K, many orders of magnitude higher than for atoms. However, it is in practice difficult to reach BEC conditions, as the temperature of excitons can considerably exceed that of the semiconductor lattice. The search for exciton BEC has concentrated on long-lived excitons: the exciton lifetime against electron–hole recombination therefore should exceed the characteristic timescale for the cooling of initially hot photo-generated excitons[4–10]. Until now, all experiments on atom condensation were performed on atomic gases confined in the potential traps. Inspired by these experiments, and using specially designed semiconductor nanostructures, we have collected quasi-two-dimensional excitons in an in-plane potential trap. Our photoluminescence measurements show that the quasi-two-dimensional excitons indeed condense at the bottom of the traps, giving rise to a statistically degenerate Bose gas.

More than three decades ago Keldysh and Kozlov[1] showed that in the dilute limit, $na_B^D \ll 1$ (a_B is the exciton Bohr radius, n the exciton density and D the dimensionality), excitons behave as weakly interacting Bose particles and are expected to undergo the Bose–Einstein condensation (BEC). Because the exciton mass, M, is very small, the three-dimensional critical temperature for exciton BEC, $T_c^{3D} = 0.527 k_B^{-1} 2\pi\hbar^2 M^{-1} (n/g)^{2/3}$ (g is the spin degeneracy of the exciton state, k_B is the Boltzmann constant), should reach several Kelvins at experimentally accessible exciton densities, that is, about six orders of magnitude higher than the critical temperature for atom BEC. The theoretical predictions for exciton BEC and

a possible crossover from exciton BEC at low densities to the Bardeen–Cooper–Schrieffer (BCS)-like condensate, the excitonic insulator, at high densities ($na_B^D \gg 1$) (ref. 11) have initiated intensive experimental studies[4,5,7,5,9–10].

In spite of the relatively high T_c, it is experimentally very difficult to lower the temperature of a high-density exciton gas enough to reach the BEC. Cooling semiconductor lattices well below 1 K is routinely achieved with He refrigerators. Nevertheless, the exciton temperature, T_X, can often considerably exceed that of the lattice. In fact, because the excitons can recombine, T_X is determined by the ratio of the exciton energy relaxation and recombination rates. Therefore, the search for BEC has concentrated on long-lived excitons: to reach low enough T_X after the initial photo-generation, the exciton gas should be given time to lower its temperature to close to that of the lattice.

Over the last two decades the experimental efforts to observe exciton BEC in bulk semiconductors dealt mainly with bulk Cu_2O (refs 4, 5), a material whose ground exciton state is optically dipole-inactive and has, therefore, a very low radiative recombination rate. The conditions necessary for realization of BEC in Cu_2O appeared to be experimentally accessible: $T_c \propto n^{2/3}$ would reach $\simeq 2.3$ K at exciton density $n = 10^{17}$ cm^{-3}. However, another, competitive density-dependent process begins at high n: the exciton Auger recombination rate, proportional to n, which increases faster than T_c with increasing n. Recent precise measurements indicate that the Auger recombination rate in Cu_2O is about two orders of magnitude higher than was assumed before and, therefore, the exciton densities reached in the up-to-date experiments are far below that

required to achieve a degenerate Bose gas of excitons[9].

In our attempt to create a degenerate Bose gas of excitons we explore another system: a quasi-two-dimensional gas of indirect excitons in coupled quantum wells (QWs)[7,10]. There are two primary advantages of using coupled QWs for realizing a quantum degenerate exciton gas and, ultimately, the BEC-like phase transition: (1) the long lifetime of indirect excitons and (2) the short exciton cooling time. The long lifetimes originate from the spatial separation between the electron and hole layers (Fig. 1a), resulting in a radiative lifetime of indirect excitons in our coupled QW samples that is more than three orders of magnitude longer than that of direct excitons in single QWs. As for the cooling of hot photoexcited excitons down to the temperatures of the cold lattice, which occurs via emission of bulk longitudinal acoustic phonons, it is about three orders of magnitude faster for excitons in GaAs QWs than that in bulk GaAs. This is due to relaxation of the momentum conservation law in the **z** direction (**z** $\perp$ QW plane). Indeed, for quasi-two-dimensional systems the ground-state mode $E = 0$ couples to the continuum of the energy states $E \geq E_0$ rather than to the single energy state $E = E_0 = 2Mv_s^2$ (v_s is the sound velocity) as it occurs in bulk semiconductors[8]. The long lifetime and the fast cooling rate of indirect excitons favour accumulation of these Bose particles in the lowest energy states and allow the photoexcited excitons to cool down to temperatures well below 1 K, where the dilute quasi-two-dimensional gas of indirect excitons becomes statistically degenerate[10].

Coupled QW structures can provide a further advantage for indirect-exciton BEC. It is worth noting here that all the recent
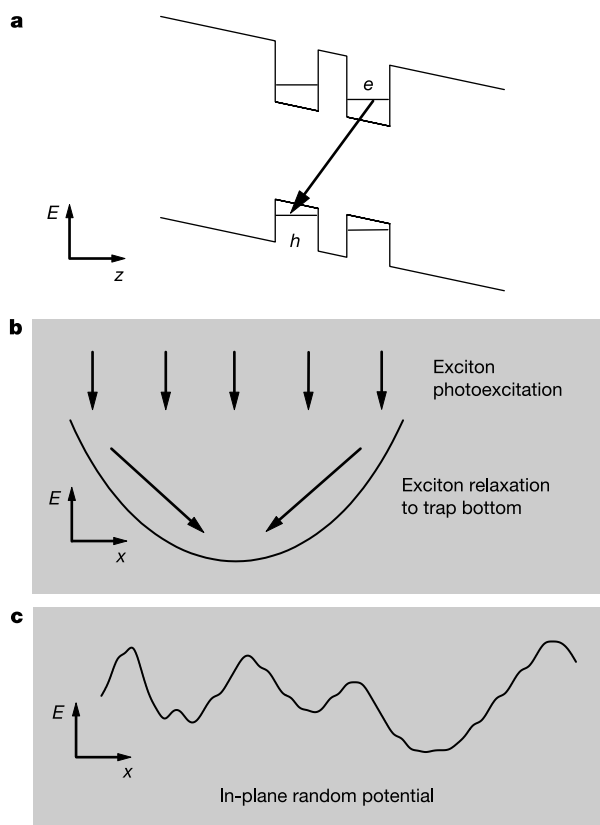

Figure 1 Potential profiles in coupled quantum well structures in the growth direction, **z**, and in the *x–y* plane. **a**, Energy band diagram of the coupled quantum well (QW) structures. The indirect excitons in coupled QWs are characterized by high cooling rates, three orders of magnitude higher than in bulk GaAs, and long lifetime, more than three orders of magnitude longer than in a single GaAs QW. The lifetime is much longer than the characteristic timescale for cooling, so that the exciton temperature can be very low, well

below 1 K. **b**, In-plane potential of a trap for excitons in QW structures. The conditions for the exciton BEC are significantly improved in such potential traps because of the confinement effect and the enhanced local density driven by the exciton energy relaxation. **c**, Schematic of the in-plane potential landscape formed by random potential fluctuations. Such natural local potential minima can host highly degenerate exciton systems and, ultimately, BEC.

advances in BEC of atoms were made possible by exploiting the confinement of atomic gases within potential traps. Similarly, the conditions for BEC of indirect excitons are significantly improved if the excitons are collected in a local minimum caused by an in-plane modulation of the potential (Fig. 1b). Then T_c increases because of confinement effects and the enhancement of the local density at the trap centre that result from the drift of photoexcited excitons toward the bottom of the trap.

In particular, in the case of confinement by an in-plane two-dimensional harmonic potential the critical temperature is:

$$T_c = \frac{1}{k_B} \frac{\sqrt{6}}{\pi} \hbar\omega \sqrt{N/g} \qquad (1)$$

where $\hbar\omega$ is the quantization energy and N is the number of excitons in the trap. In the case of confinement by an in-plane square potential (two-dimensional box):

$$T_c = \frac{4\pi\hbar^2 n}{2Mgk_B} \frac{1}{\ln(nS/g)} \qquad (2)$$

where S is the area of the box[12]. We note that the T_c given by these two equations vanishes either when $\hbar\omega \to 0$ or when $S \to \infty$, thus reproducing the well-established results that in infinite ideal two-dimensional systems BEC is only possible at $T = 0$. In such a system, however, a phase transition to a superfluid exciton state is still possible at finite temperatures[13]. As for atomic systems, excitons condense in real space in the lowest energy state at the bottom of the trap, which corresponds to the condensation in momentum space for infinite systems, that is, to the BEC.

Semiconductor technology allows us now to engineer the in-plane potential for indirect excitons in nanostructures. For example, traps can be formed by lateral modulation of the electric field along $\mathbf{z}$, E_z, by application of a local stress or of a local magnetic field. Besides this interesting approach intrinsic local minima of the in-plane potential are always present in any QW structure. These natural traps are caused by random fluctuations of the interfaces, for example, QW thickness and/or alloy disorder, or E_z (see Fig. 1c). Such potential minima can host highly degenerate exciton systems and ultimately BEC[6,7]. There is a great variety of fluctuations (such as in width and depth) in the random potential of any semiconductor heterostructure. Therefore, among all the many traps present in a given sample, the exciton gas will, by itself, select those with optimal parameters for condensation: this is an important advantage of the natural traps. A clear signature of condensation of a degenerate exciton gas in such a trap is its strongly in-plane localized photoluminescence (PL) emission peaked at the bottom
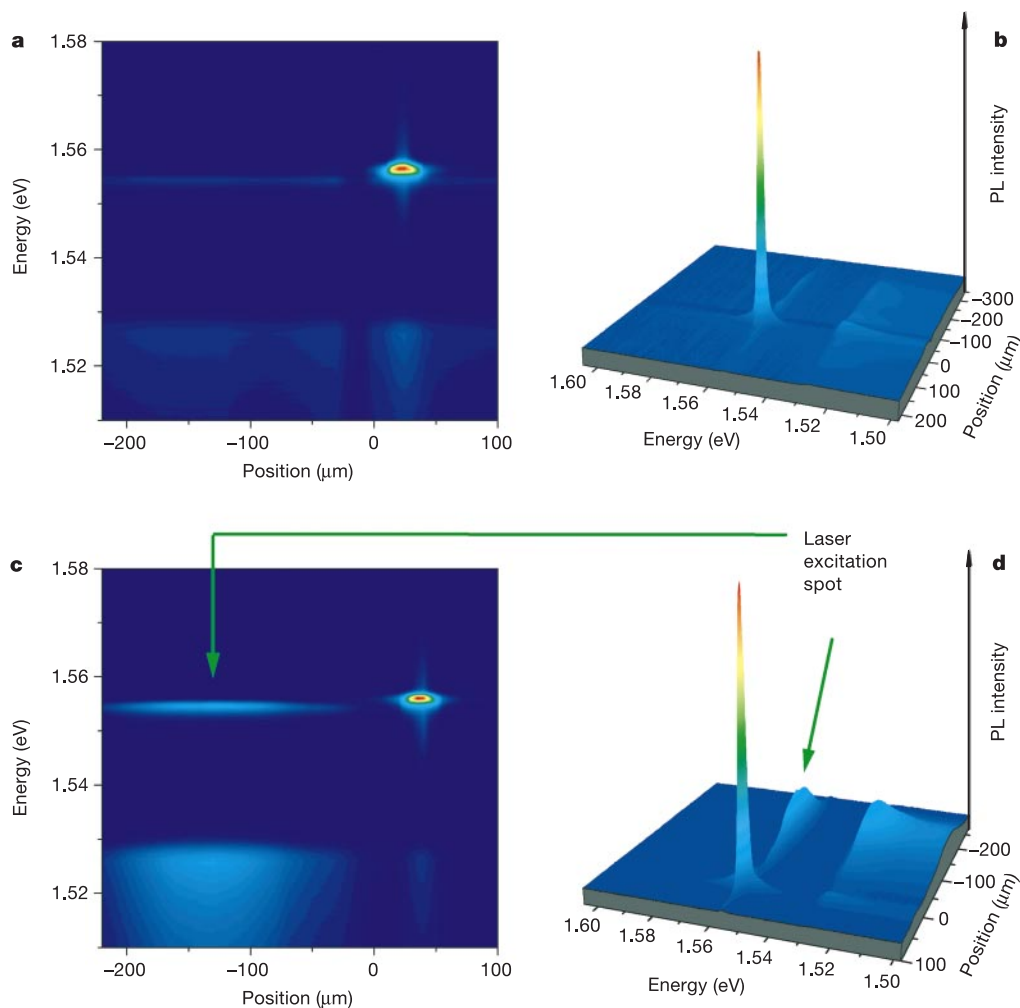

Figure 2 Photoluminescence intensity versus energy and one of the in-plane coordinates x at $T = 1.6\,\text{K}$ (the photoluminescence (PL) variation along the orthogonal in-plane coordinate y is the same). The indirect exciton PL line is at about 1.555 eV; the broad line below 1.53 eV comes from the bulk n^+-GaAs emission. **a**, **b**, The laser excitation spot is defocused and excites the whole $500 \times 500\,\mu\text{m}^2$ mesa. The indirect excitons are collected in a natural trap resulting in a PL intensity at its centre about 30 times higher than outside. **c**, **d**, The laser excitation is focused to a spot around $100 \times 200\,\mu\text{m}^2$ about 170 μm away from the trap. Even in these conditions the indirect exciton PL intensity at the trap centre is about six times larger than at the centre of the excitation spot. This demonstrates drift and condensation of indirect excitons over macroscopic distances.

of the trap.

Here we report the first observation of the condensation of indirect excitons in natural traps, where a highly statistically degenerate Bose gas of indirect excitons builds up. We have performed spectrally and spatially resolved PL, monitoring both the indirect and direct exciton emissions. This enables us to compare, under identical experimental conditions, the anomalous behaviour of the former and the regular behaviour of the latter (for details see Methods section). Using a spatial resolution of 10 μm at $T = 1.6$ K, we have observed a huge local enhancement of the indirect exciton PL intensity in several $500 \times 500\,\mu m^2$ mesas. We interpret this effect by the effective accumulation of excitons in specific natural traps. Depending on the location on the wafer, the mesas can exhibit no trap, one trap or two traps. In a given sample the position of traps is well-defined and all experimental results are extremely robust: for example, they are reproducible after cycling the sample temperature up to room temperature and back to 1.6 K many times. Study of the spatial dependence of the PL intensity along two orthogonal in-plane directions, **x** and **y**, indicates that the exciton clouds in the traps have a nearly circular shape.

As shown in Fig. 2a and b, under uniform excitation of a whole mesa using a defocused laser, the indirect exciton PL intensity at the centre of a trap is about 30 times higher than that emitted from any other location on the mesa outside the trap. This clearly demonstrates that the indirect excitons collect at the centre of the trap, where their concentration is strongly enhanced. We estimate the density of indirect excitons in the uniformly illuminated mesas, far from the traps, to be $n_{avg} \approx 3 \times 10^9\,cm^{-2}$. This value, using the PL

intensities ratio for the exciton density in the traps yields: $n_{trap} \approx 10^{11}\,cm^{-2}$. In Fig. 2a and b the full width at half maximum (FWHM) of the profile of the exciton cloud in the trap is 23 μm; thus, the total number of excitons it contains is $N = nS \approx 4 \times 10^5$.

We have also explored the traps under inhomogeneous excitation using a smaller laser spot, $100 \times 200\,\mu m^2$, that can be located anywhere on the mesa as far away from a trap as 400 μm. As seen in Fig. 2c and d, even in that case the indirect excitons are collected by the trap and the PL intensity from the trap is up to about six times higher than the PL intensity in the excitation spot. The long exciton lifetime and large diffusion coefficient allow the indirect excitons to travel several hundred micrometres and to be collected by the trap. During their travel the initially hot excitons, photoexcited at high energy, effectively thermalize down to the lattice temperature via photon emission. Therefore, in the case of remote excitation the trap is filled by the cold excitons. This is confirmed by the disappearance of the PL emission line of the hot direct excitons from the spectrum in the trap, although that line is present in the spectra at the excitation spot. In this case the exciton density in the laser spot is $n_{spot} \approx 2 \times 10^{10}\,cm^{-2}$, which implies $n_{trap} \approx 1.2 \times 10^{11}\,cm^{-2}$ in the trap. This value is similar to that obtained in experiments with defocused laser excitation discussed above. In Fig. 2c and d the FWHM of the profile of the exciton cloud in the trap is 20 μm so that $N = nS \approx 4 \times 10^5$.

Assuming that one can apply the thermodynamic equilibrium description of ideal point-like bosons to indirect excitons and a two-dimensional box shape for the trap, equation (2) with the GaAs parameters $g = 4$ and $M = 0.21m_0$ (m_0 is the free electron mass[14])
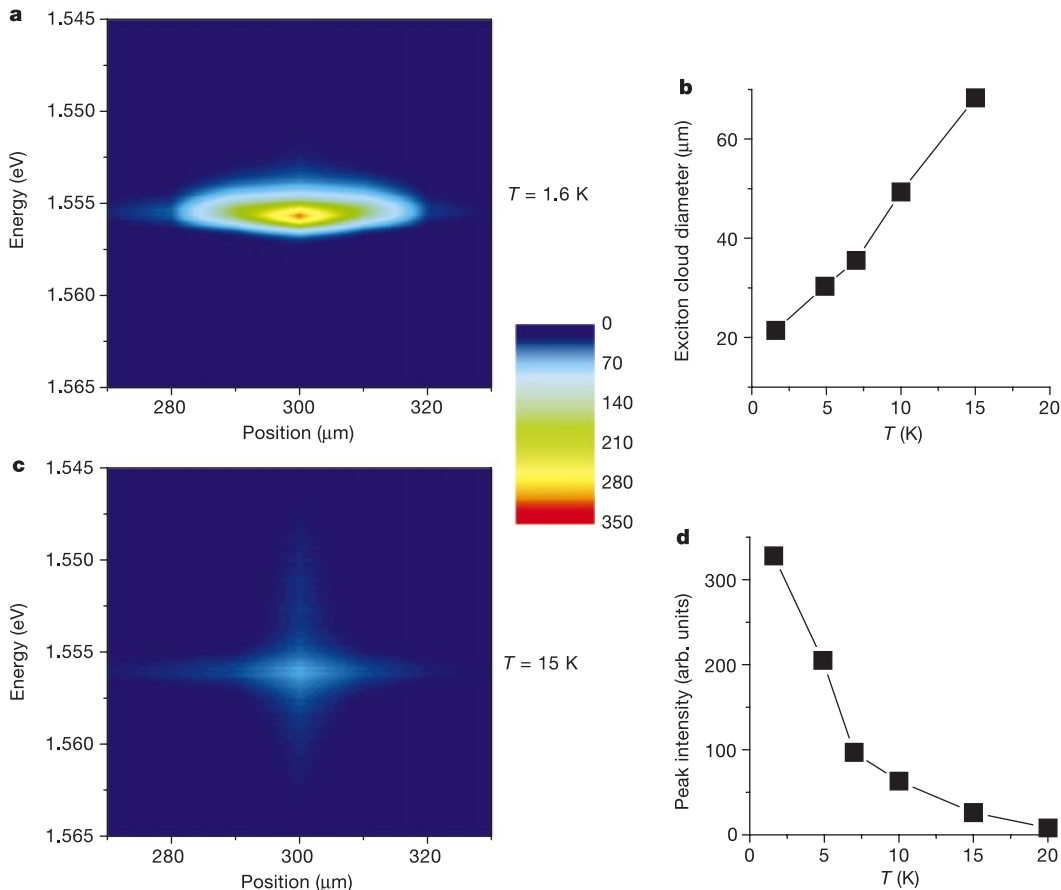

Figure 3 The spatial shrinkage of the exciton cloud near the bottom of the potential trap as the temperature is reduced. **a**, **c**, Contour map of the indirect exciton PL intensity versus the in-plane coordinate x and energy at $T = 1.6$ K (**a**) and $T = 15$ K (**c**). The temperature

dependence of the diameter of the indirect exciton cloud and their PL peak intensity are shown in **b** and **d**. As the temperature is reduced the indirect excitons condense at the bottom of the trap.

gives an estimate for the critical temperatures for exciton BEC in the trap of $T_c \approx 0.5$ K and $T_c \approx 0.7$ K, for the uniform and remote excitations respectively. These crude estimates imply that in our current experiments with $T_{bath} = 1.6$ K the conditions for exciton BEC are still not achieved. We note, however, that many factors are disregarded in the estimate; in particular, the indirect excitons are not ideal bosons—on the contrary, they are characterized by a nonlocal repulsive interaction that reinforces condensation and should result in an increase of T_c (ref. 15). In the remote excitation experiments the degenerate Bose gas of indirect excitons builds up outside the trap in the excitation spot, as revealed by the bosonic stimulation of exciton scattering to the low-energy states (similar to experiments in ref. 10). The degree of quantum degeneracy is much higher for indirect excitons accumulated at the centre of the trap.

The diameter of the exciton cloud near the bottom of the potential trap reduces as the temperature is lowered, while the peak intensity increases, as shown in Fig. 3. This demonstrates that while at high temperatures the excitons are distributed over the high energy states of the trap, at low temperatures the excitons condense at the bottom of the trap. Similar spatial shrinkage of atom clouds is characteristic of atomic BEC in the potential traps.

Direct excitons, however, exhibit none of the collection effects which influence the indirect excitons so strongly. This is consistent with a high temperature of direct excitons: the short lifetime does not allow an effective cooling of direct excitons. Furthermore, that short lifetime limits the distance they can travel before annihilation, making collection effects on large length scales impossible for direct excitons.
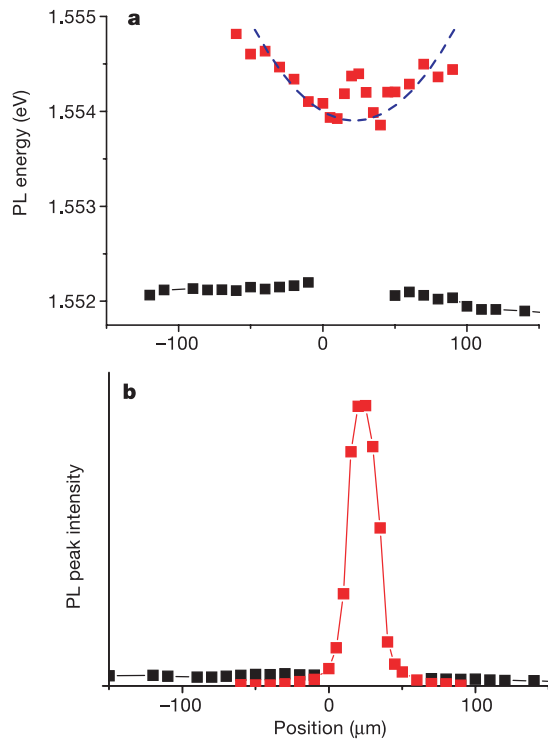
In Fig. 4 we show how the PL of optically active indirect excitons varies with the distance ρ from the centre of the trap. The PL emission energy exhibits several anomalies. First, the energy is higher inside the trap than outside by $\Delta E_{PL} \approx 2$ meV. This difference remains practically constant when the indirect exciton energy inside and outside the trap are reduced by increasing E_z: the trap looks like a 'levitating bowl'. This raises several interesting issues for future studies: (1) Although ΔE_{PL} is much smaller than the initial energy of the photoexcited indirect excitons, how can the trap collect these indirect excitons despite a non-negligible energy barrier at its edges? (2) The indirect exciton energy in the trap can be limited by its depth in analogy with the case of atom evaporative cooling in optical traps. Second, the PL emission energy exhibits a bump at the centre of the trap, $\delta E_{PL} \approx 0.5$ meV, which increases with the density of indirect excitons. We tentatively explain such a 'Mexican hat' structure by the pressure induced by the stimulated flux of excitons towards the centre of the trap. The microscopic origin of the trap is not essential. The only important point is that in the fluctuating in-plane potential landscape of the sample the exciton gas finds spontaneously those local minima with optimal parameters for condensation. The possibility of evaporative cooling could be important in the potential minimum selection. Modelling the overall trap profile by the harmonic potential shown by the blue dashed line in Fig. 4, equation (1) with $N = 4 \times 10^5$ gives, for the 'ideal boson' case, $T_c \approx 1.0$ K, close to the two-dimensional box value. □

Methods

n^+–i–n^+ GaAs/AlGaAs coupled QW structure was grown by MBE. The i-region consists of two 8-nm GaAs QWs separated by a 4-nm $Al_{0.33}Ga_{0.67}As$ barrier and surrounded by two 200-nm $Al_{0.33}Ga_{0.67}As$ barrier layers. The electric field in the **z**-direction is monitored by the external gate voltage V_g applied between the highly conducting n^+-layers. The narrow PL linewidth, about 1 meV, indicates small in-plane disorder. The sample was excited with a HeNe laser, wavelength $\lambda = 632.8$ nm and power $P = 3$ mW. The experiments were performed in a ^{4}He cryostat with optical windows. A spatial resolution of 10 μm was achieved using a pinhole in the intermediate image plane. For $V_g \approx 0$ the ground state of the optically pumped coupled QW is a direct exciton made of an electron and a hole in the same layer and similar to the excitons in single QWs. For nonzero V_g the ground state is an indirect exciton made of an electron and a hole in different layers (Fig. 1a). The indirect excitons have a permanent dipole along **z** and thus exercise on each other a repulsive interaction—their energy therefore increases with density. The corresponding energy shift, $\delta E(n)$, allows us to evaluate their concentration using $\delta E(n) = 4\pi ne^2 d/\epsilon$, where d is the effective separation between the electron and hole layers and ϵ is the dielectric constant. For the strongest excitations in the experiments reported here excitation density $W = 10$ W cm^{-2} and maximum density $n_{max} \approx 2 \times 10^{10}$ cm^{-2} at the centre of the excitation spot. Radiative recombination is the dominant decay mechanism of indirect excitons in our high-quality sample. The spatially resolved PL kinetics shows that the excitons in the centre of the trap have a lifetime as long as the excitons outside the trap. The energy of the trapped excitons varies with applied electric field similar to that of the excitons outside the trap, thus proving unambiguously that the long-lived indirect excitons are those that condense at the bottom of the trap.

Figure 4 Anomalous properties of the traps revealed by the spatial dependence of the indirect exciton photoluminescence. The energy of the PL peak is higher in the trap than outside; although at large distances from the centre, ≥ 10 μm, the PL energy indicates that the potential in the trap has an overall bowl-like shape, it exhibits a 0.5-meV bump near the centre that increases with density, $T = 1.6$ K. **a**, **b**, Red (black) squares present the indirect exciton emission energies (**a**) and intensities (**b**) in (out of) the potential trap. Both emission lines are resolved near the trap edge. The blue dashed line is a guide for the eyes and represents a parabolic profile.

1. Keldysh, L. V. & Kozlov, A. N. Collective properties of excitons in semiconductors. *Zh. Eksp. Teor. Fiz.* **54**, 978–993 (1968); *Sov. Phys. JETP* **27**, 521–528 (1968).
2. Anderson, M. N., Ensher, J. R., Matthews, M. R., Wieman, C. E. & Cornell, E. A. Observation of Bose–Einstein condensation in a dilute atomic vapor. *Science* **269**, 198–202 (1995).
3. Davis, K. B. *et al.* Bose–Einstein condensation in a gas of sodium atoms. *Phys. Rev. Lett.* **75**, 3969–3973 (1995).
4. Snoke, D. W., Wolfe, J. P. & Mysyrowicz, A. Quantum saturation of a Bose gas: excitons in Cu₂O. *Phys. Rev. Lett.* **59**, 827–830 (1987).
5. Lin, J. L. & Wolfe, J. P. Bose–Einstein condensation of paraexcitons in stressed Cu₂O. *Phys. Rev. Lett.* **71**, 1222–1225 (1993).
6. Zhu, X., Littlewood, P. B., Hybertsen, M. & Rice, T. Exciton condensate in semiconductor quantum well structures. *Phys. Rev. Lett.* **74**, 1633–1636 (1995).
7. Butov, L. V. & Filin, A. I. Anomalous transport and luminescence of indirect excitons in AlAs/GaAs coupled quantum wells as evidence for exciton condensation. *Phys. Rev. B* **58**, 1980–2000 (1998).
8. Ivanov, A. L., Littlewood, P. B. & Haug, H. Bose–Einstein statistics in thermalization and photoluminescence of quantum well excitons. *Phys. Rev. B* **59**, 5032–5048 (1999).
9. O'Hara, K. E., Súilleabháin, L. Ó. & Wolfe, J. P. Strong nonradiative recombination of excitons in Cu₂O and its impact on Bose–Einstein statistics. *Phys. Rev. B* **60**, 10565–10568 (1999).
10. Butov, L. V. *et al.* Stimulated scattering of indirect excitons in coupled quantum wells: Signature of a degenerate Bose-gas of excitons. *Phys. Rev. Lett.* **86**, 5608–5611 (2001).
11. Keldysh, L. V. & Kopaev, Yu. V. Possible instability of the semimetallic state toward Coulomb interaction. *Fizika Tverdogo Tela* **6**, 2791–2798 (1964); *Sov. Phys. Solid State* **6**, 2219–2224 (1965).
12. Ketterle, W. & van Drutten, N. J. Bose–Einstein condensation of a finite number of particles trapped in one or three dimensions. *Phys. Rev. A* **54**, 656–660 (1996).

13. Popov, V. N. On the theory of the superfluidity of two- and one-dimensional Bose systems. *Theor. Math. Phys.* **11**, 565–573 (1972).

14. Butov, L. V., Mintsev, A. V., Lozovik, Yu. E., Campman, K. L. & Gossard, A. C. From spatially indirect to momentum-space indirect exciton by in-plane magnetic field. *Phys. Rev. B* **62**, 1548–1551 (2000).

15. Leggett, A. J. Bose–Einstein condensation in the alkali gases: Some fundamental concepts. *Rev. Mod. Phys.* **73**, 307–356 (2001).

Competing interests statement

The authors declare that they have no competing financial interests.

Correspondence and requests for materials should be addressed to L.V.B. (e-mail: LVButov@lbl.gov).

....

All-metallic three-dimensional photonic crystals with a large infrared bandgap

J. G. Fleming*, S. Y. Lin*, I. El-Kady†, R. Biswas & K. M. Ho†

* MS 0603, Sandia National Laboratories, PO Box 5800, Albuquerque, New Mexico 87185, USA

† Ames Laboratory, Department of Physics and Astronomy, Iowa State University, Ames, Iowa 50011, USA

....

Three-dimensional (3D) metallic crystals are promising photonic bandgap[1–3] structures: they can possess a large bandgap[4–6], new electromagnetic phenomena can be explored[7–9], and high-temperature (above 1,000 °C) applications may be possible. However, investigation of their photonic bandgap properties is challenging, especially in the infrared and visible spectrum, as metals are dispersive and absorbing in these regions[10]. Studies of metallic photonic crystals have therefore mainly concentrated on microwave and millimetre wavelengths[8,11,12]. Difficulties in fabricating 3D metallic crystals present another challenge, although emerging techniques such as self-assembly[13,14] may help to resolve these problems. Here we report measurements and simulations of a 3D tungsten crystal that has a large photonic bandgap at infrared wavelengths (from about 8 to 20 μm). A very strong attenuation exists in the bandgap, ~30 dB per unit cell at 12 μm. These structures also possess other interesting optical properties; a sharp absorption peak is present at the photonic band edge, and a surprisingly large transmission is observed in the allowed band, below 6 μm. We propose that these 3D metallic photonic crystals can be used to integrate various photonic transport phenomena, allowing applications in thermophotovoltaics and blackbody emission.

The tungsten 3D photonic crystal was made by selectively removing Si from already fabricated polysilicon/SiO₂ structures, and back-filling the resulting mould with chemical vapour deposited (CVD) tungsten. This method could be extended to create almost any 3D single-crystal metallic photonic crystal at infrared wavelengths; such photonic crystals have not previously been achievable. Scanning electron microscope (SEM) images of the fabricated four-layer 3D tungsten photonic crystal are shown in Fig. 1a and b.

The optical properties of the 3D tungsten photonic crystal were characterized using a Fourier-transform infrared measurement system for wavelengths λ ranging from 1.5 to 25 μm (ref. 15). To obtain reflectance (R), a sample spectrum was taken from a 3D tungsten crystal, and then normalized to a reference spectrum of a uniform silver mirror. To find the absolute transmittance (T), a transmission spectrum taken from a 3D tungsten crystal sample was normalized to that of a bare silicon wafer. This normalization procedure is intended to calibrate away extrinsic effects, such as light reflection at the air–silicon interface and silicon absorption. For tilt-angle transmission measurements, the sample was mounted onto a rotational stage with rotational angles θ ranging from 0° to 60°, measured from the surface normal—that is, the ⟨001⟩ direction.

In Fig. 2a we show the absolute reflectance (black diamonds), transmittance (small black circles) and absorptance (red circles) of a four-layer 3D tungsten photonic crystal. Light propagates along the ⟨001⟩ direction of the crystal and is unpolarized. The reflectance exhibits oscillations at λ < 5.5 μm, rises sharply at λ ≈ 6 μm (the band edge) and finally reaches a high reflectance of 90% for λ > 8 μm. Correspondingly, the transmittance shows distinct peaks at λ < 5.5 μm, decreases sharply at λ ≈ 6 μm (the photonic band edge) and then decreases to below 1% for λ > 8 μm. The dashed line in Fig. 2a is for reference purposes, and shows the transmittance of a 6,000-Å uniform tungsten film. The simultaneous high R and low T at λ > 8 μm is indicative of the existence of a photonic bandgap in the tungsten 3D photonic crystal. The attenuation is as large as ~30 dB at λ = 10 μm for our four-layer sample, or equivalently a unit cell. The multiple oscillations at λ < 5.5 μm are attributed to photonic density-of-states (DOS)
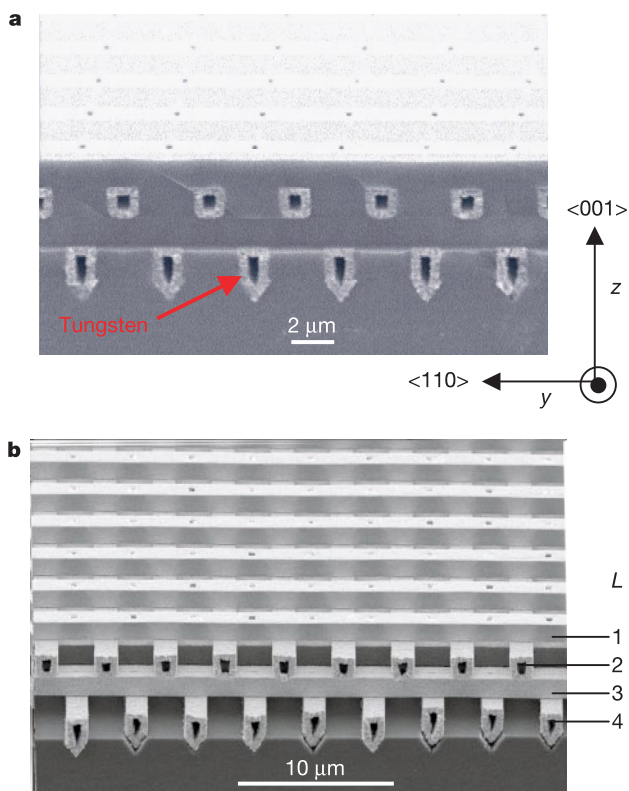
Figure 1 Images of a 3D tungsten photonic crystal, taken by a scanning electron microscope (SEM). The images taken with and without oxide are shown in **a** and **b**, respectively. The 1D tungsten rod is 1.2 μm wide, the rod-to-rod spacing is 4.2 μm and the filling fraction of tungsten material is 28%. The bottom 'V' groove is formed owing to a slow KOH etching {111} planes of the (001) oriented silicon substrate. The step coverage of the deposition process is not 100%, and this gives rise to the formation of a keyhole in the centre of the more deeply imbedded lines.